

# Numerical Analysis of Concrete Composites at the Mesoscale Based on 3D Reconstruction Technology of X-ray CT Images

C.B. Du<sup>1,2</sup>, S.Y. Jiang<sup>2</sup>, W. Qin<sup>3</sup> and Y.M. Zhang<sup>2</sup>

**Abstract:** A numerical analysis of concrete composites at the mesoscale based on three-dimensional (3D) reconstruction technology of X-ray computed tomography (CT) images is presented in this paper. For X-ray CT images of concrete, morphology processing was used to recover complete image information, including borders, and the median filtering method was applied to eliminate potential impurities in the images. The final X-ray CT images obtained after processing for a concrete section were composed of three-value pixels that indicated aggregate particles, mortar matrix and air voids, and the 3D structure of the concrete specimen was reconstructed using the volume data method. The mapping mesh method was used to identify element material attributes, and a four-point bending-tension fracture process for the specimen was performed. The numerical results show that the load-displacement curve and failure crack location from the reconstructed model were similar to those from the experiment. The damage development for each phase of material obtained from the numerical results indicates that crack initiation occurs in the interface transition zone (ITZ); one macro crack is formed at final failure, and it is caused by the growth and propagation of the micro cracks.

**Keywords:** Concrete composites, X-ray CT, 3D reconstruction, Nonlinear FEM

## 1 Introduction

At the mesoscale, concrete is a multiphase composite material consisting of mortar matrix, aggregate particles, interface transition zone (ITZ) and air voids. To reveal the failure mechanism of concrete, its composite behaviour may be studied analytically using the mesoscopic approach. It is necessary that a concrete numerical model for mesoscopic mechanics numerical analysis be constructed. The model

---

<sup>1</sup> Corresponding author. Email:cbdu@hhu.edu.cn.

<sup>2</sup> Mechanics and Materials Experiment Center, Hohai University, Nanjing 210098, China.

<sup>3</sup> CCCC Third Harbor Consultants Co., Ltd, Shanghai 200032, China.

has a great influence on the numerical simulation results (Wittmann, Roelfstra, and Sadouki, (1985)).

In the past two decades, many scholars have proposed random concrete models based on real aggregate shape and distribution rules. Wang, Kwan, and Chan (1999) presented a way to generate a two-dimensional random aggregate structure for rounded and angular aggregates based on the Monte Carlo random sampling principle and developed a method of mesh generation using the advancing front approach. Garboczi and Bullard (2004) described the aggregate shape using spherical harmonics to generate an aggregate model that is similar to the shape of natural stone. To obtain a higher aggregate content, Wriggers and Moftah (2006) proposed a packing algorithm, and the numerical simulation results were compared with experimental results to test the model accuracy. Du and Sun (2007) presented a practical method for modelling the arbitrary shapes of two-dimensional concrete. In their proposed method, all random triangular fundamental aggregates of the same type are generated at one time, and then two-dimensional arbitrary shape aggregates are generated by the random extension method. Their algorithm is superior to common methods, in which all aggregates are generated individually. The aggregate volume fractions reached 60%–70% in their study. A new computer simulation method was also proposed for the random packing of particles with variable sizes in three-dimensional (3D) space (Fu and Dekelbab (2003)). This method consists of two steps: kinematics simulation and dynamics simulation. The kinematics simulation uses a 3-D cellular registration system for efficient particle deposition. The dynamics simulation models further packing of the matrix of particles using the discrete element method (DEM). In another paper, a modified ellipsoid function was adopted to represent the aggregate shape (Häfner, Eckardt, Luther and Könke (2006)), and the effective Young's modulus of two-dimensional concrete was studied using the linear finite element method. More recently, polyhedrons were created by extending triangular fundamentals and were treated as visualised aggregates after passing through convex control and sharpness judgment (Xu, Yang, Yin, Yang and Ye(2010)), and effective elastic properties and creep under uniaxial compression were simulated. The sequential packing algorithm (SPA) was developed to model the dense packing of large assemblies of particulate materials (Sobolev and Amirjanov (2010)), and a genetic algorithm (GA) search was introduced to increase the volume of particles. Conventional discrete element simulation (DES) was used to generate numerical concrete (He, Guo, Stroeven, Stroeven and Sluys (2009)). However, there are two drawbacks to these models: the aggregate shape and distribution in each model are different from those in real concrete, and the aggregate content in the model is lower than that in real concrete. These drawbacks cause differences between the mechanical properties of the numerical and experimental

results.

With the development of image processing techniques and image acquisition equipment, concrete models using image reconstruction have developed rapidly. By comparing different methods, such as the X-ray CT method, the thermal infrared method, the microwave method, and the acoustic emission method, Buyukozturk (1998) found that the X-ray CT method is an effective way to study the internal structure of concrete. Moar, Kwan and Chan (1998) studied the application of digital image processing to aggregate generation. John and Denis (2001) found that the digital image correlation technique (DIC) can be used to observe small surface cracks in concrete but that the X-ray CT method is better for large internal cracks. They also discussed the influences of aggregate shape and crack shape on concrete strength and toughness according to CT images obtained after concrete rupture. Yang and Buenfeld (2001) found a way to obtain aggregate elements from photographs by processing the photographs from scanning electron microscopy (SEM). Saadeh, Al-Rousan, Garboczi and Little (2005) and Cheok, Stone and Garboczi, (2006) used X-ray CT to study the shape characteristics of natural stone. Tian, Dang, Liang and Chen (2008) studied the mesoscopic damage process of concrete using CT image information. It should be mentioned that some significant works also cover non-concrete materials in applying X-ray CT technology, such as wood composites (Evans, Morrison and Senden *et al.* 2010), macroporous alumina (Andersson, Jones, Knackstedt and Bergström 2010), and porous materials (Madadi, Jones, Arns and Knackstedt 2009) in which the 3D CT is applied together with numerical simulations based on the finite element method to estimate the properties of porous materials. However, because of the difficulty and complexity of the reconstruction of 3D concrete, there are still many details of the mesoscopic structure and analysis that need to be studied more fully.

This paper is composed of four parts. The first part describes the X-ray CT image processing, including recovery of complete image information and filtering and elimination of noise. The second part describes the application of the 3D reconstruction technology to concrete. The third part describes the measurement of the failure process of a four-point flexural-tensile concrete specimen and the numerical simulation using a reconstruction model based X-ray CT technology, and the accuracy of the simulation is discussed. Conclusions are drawn in the fourth part.

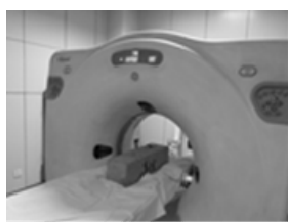
## **2 X-ray CT image processing**

### ***2.1 Composition of concrete specimens***

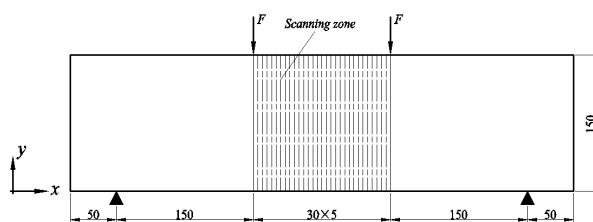
Concrete specimens with dimensions of 150 mm × 150 mm × 550 mm were poured in the laboratory. The composition of the concrete specimens was designed

according to the real composition of the three-graded dam concrete used in the JINPING project (Xu, Tang, Li, Zhou, Sha, Liang and Yang(2011)). The mass proportion of the coarse aggregate, medium aggregate and fine aggregate of the three-grade dam concrete was 4:3:3. The diameter intervals of the coarse aggregate, medium aggregate and fine aggregate was 40–80 mm, 20–40 mm, and 5–20 mm, respectively. To pour the small concrete specimens, the coarse aggregate was removed. Therefore, the concrete specimens only contain medium aggregate and fine aggregate with a 1:1 proportion. The ratio of water to cementations material was 0.39. The aggregate density was  $2800 \text{ kg/m}^3$ . The aggregate volume content was 40%. The detailed composition is given in Tab.1.

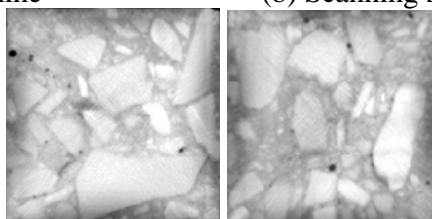
## 2.2 X-ray CT slices of concrete specimens



(a) X-ray CT machine



(b) Scanning zone (mm)



(c) X-ray CT slices of a concrete specimen

Figure 1: Acquisition of X-ray CT slices

A medical CT machine was used to collect X-ray CT slices of the concrete specimens because of the restrictions of the experimental conditions. The CT machine used was a GE HISPEED FX/I spiral CT machine. Considering the size of the concrete fine aggregate and the accuracy of the CT machine, a 5-mm scanning interval for a mid-span with a length of 150 mm was used, as shown in Figs. 1(a) and 1(b). That was we could acquire a CT slice per 5 mm for a mid-span with a length of 150 mm, so totally 31 CT slices were obtained in the scanning zone. Original images were obtained in the Digital Imaging and Communication in Medication (DICOM) format. Multiple digital photos  $300 \times 300$  pixels in size were obtained using the

Table 1: Material composition of the concrete specimens

| Composition  | Composition  |
|--|--|
| $\text{Fly ash content}(\%) = \frac{\text{Fly ash weight}}{\text{Cement + Fly ash weight}} \times 100\%$ | 35   |
| $\text{Sand ratio}(\%) = \frac{\text{Sand volume}}{\text{Sand volume + Gravel volume}} \times 100\%$     | 21   |
| Water (kg/m <sup>3</sup> )   | 148.2  |
| Cement (kg/m <sup>3</sup> )  | 247  |
| Fly ash (kg/m <sup>3</sup> )   | 133  |
|  | $\text{Water reducing agent dosage} (\%) = \frac{\text{Water reducing agent weight}}{\text{Cement weight}} \times 100\%$ |
|  | $\text{Air content}(\%) = \frac{\text{Air volume}}{\text{Concrete volume}} \times 100\%$                                 |

**Note:** The unit kg/m<sup>3</sup> is not a density unit, but denotes the mass per 1 cubic meter of concrete.

image processing software; two are shown in Fig. 1(c).

### 2.3 Preprocessing of X-ray CT images

The scanning path of the CT machine is circle, but the concrete specimen is the rectangular sample. This fact causes that the brightness of the border was lower than that of the centre. Thus, the greyscale value of the border of an image was much smaller than that of the centre. This usually caused image border distortion or some loss of information, as shown in Fig. 2. The first work in reconstructing the concrete 3D structure was to recover the border of the image and then enhance the signal-to-noise ratio (SNR) to filter and eliminate the effect of noise.



Figure 2: Distorted border

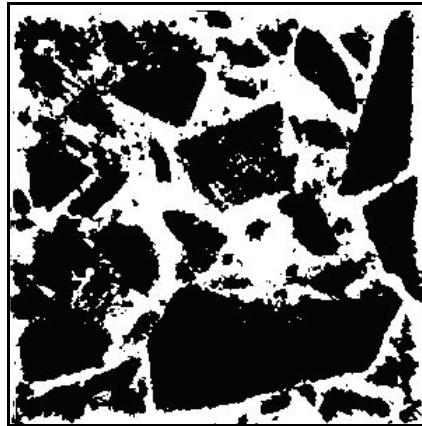


Figure 3: Image after the close operation

#### 2.3.1 Recovery of the border of an image

To avoid image border distortion, a morphology process based on expansion and erosion algorithms was used to further process the images to eliminate redundant information in the image boundaries. Expansion can lengthen and thicken objects in images; erosion can shrink and thin them (Gonzalez, Woods, and Eddins (2009)). Performing expansion or erosion directly on an image cannot solve all of the problems, and it may even introduce more errors in the boundary. Therefore, a combination of expansion and erosion operations was used. An 'open operation' is defined as erosion applied first, followed by expansion through structural elements. Object regions without structural elements can be deleted, and their contours can be smoothed. A 'close operation' is defined as expansion applied first followed

by erosion through structural elements. Thus, narrow gaps can be connected, and holes that are smaller than the structuring elements can be filled. In this paper, the structural element was configured using the IPT function *strel* in MATLAB. The capability of the function “*strel*” is to create morphological structuring element. Fig. 3 shows an image after the close operation.

### 2.3.2 Filtering and elimination of noise

The image of the subsection transformation must be filtered, and the noise must be eliminated to remove any potential impurities in regions corresponding to aggregate particles and mortar matrix. Through the disposal of these potential impurities, the regions corresponding to aggregate particles and mortar matrix can become a continuous and single-valued massive area. Therefore, the purpose of the filtering process is to recover the interior information of the two regions and to smooth the boundary between them. In this paper, a filtering method in the spatial domain was used, and median filtering was selected to eliminate noise. Four typical digital images corresponding to the first section, the section at 1/3 of the scanned length, the section at 2/3 of the scanned length, and the last section of the scanned zone are shown in Fig. 4. Black indicates aggregate particles, grey indicates mortar matrix, and white indicates air voids.

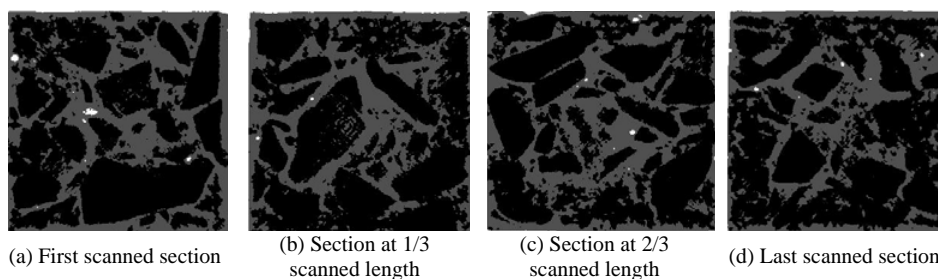


Figure 4: Final images of the four sections

## 3 3D reconstruction technology using X-ray CT Slices

Aggregate particles, mortar matrix, and air voids were identified using the method described in Section 2. The method of volume data was used to reconstruct 3D images, and element material attributes were assigned using the mapping method.

### 3.1 3D image reconstruction

Volume data with a certain resolution were established using a series of 2D images. According to different data descriptions, 3D visual methods are of three types (Shahidi, Tombropoulos, and Grzeszczuk (1998)): the surface drawing method, the volume drawing method and the mixed drawing method. The simple surface drawing method was used in this study to obtain the interface between the aggregate phase and the mortar phase and finally to extract the aggregate phase. The detailed procedure is given as follows:

1. Encapsulation of the 3D volume data  
The data from 31 preprocessed CT images (for one specimen), each image having a 2D matrix of  $300 \times 300$  pixels, were input. Then, 3D data for  $300 \times 300 \times 31$  pixels were obtained.
2. Optimisation of the 3D volume data field  
The 3D volume data field obtained always contained too much data to write in the memory of the computer. A 'reduce volume' function in MATLAB was used to decrease the amount of data, and a compressibility vector [3, 3, 1] was used.
3. Drawing of the contour surface of the 3D data field  
The interface between the aggregate phase and the mortar phase was a contour surface with a colour between grey and white. The greyscale value of the contour surface was defined as 245, the points whose grey value was 245 in the 3D data field were connected to fit an isoline, and finally, the entire contour surface was obtained. The isosurface extractor that is *Isosurface* function in MATLAB was used to obtain the point and surface data. The *Patch* function, whose capability is create patch, was used to classify subareas of the images and define the colours and brightness of the images.
4. Drawing of the boundary  
The *Isocaps* function in MATLAB was used to obtain the geometric boundaries of the 3D images, and the *Patch* function was used to define the colours and brightness of the boundaries.
5. Optimisation of the surface effect  
The contour surface obtained using this procedure consisted of many triangles; the surface was very rough where the curvature was large. The *Isonormals* function was used to calculate the normal direction of each subarea top, and the curvature surface of each aggregate was smoothed to nearly the real

aggregate shape. The effect of using the Isonormals function is shown in Figs. 5 and 6.



Figure 5: Result without smoothing

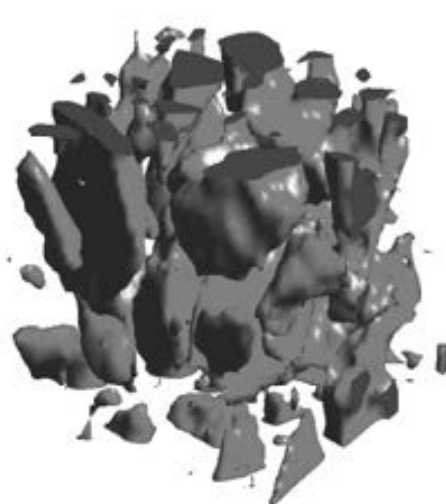


Figure 6: Result with smoothing

### ***3.2 3D FEM based on the mapping mesh method***

It is very difficult to strictly divide the concrete into elements according to each phase's boundaries in 3D concrete. The mapping mesh method was used, and the basic element model was used to describe the complex inhomogeneous structure of the specimens of 3D concrete. Using the basic element model, a concrete specimen was automatically divided into regular 8-node hexahedrons with sides of 5 mm. Fig. 7 presents the element mesh for the heterogeneous part of the four-point bending beam.

To get more useful material zones, 12 control factors, including 4 nodes (1, 2, 3, 4), 4 mid points (5, 6, 7, 8), 1 central point (9), a mortar area (10), an aggregate area (11), and an air void area (12) were considered for each scanning section in an element, as shown in Fig. 8. There were 24 control factors for an element. Four-phase materials, including aggregate particles, mortar matrix, ITZ and an air void, were considered. The detailed determination of material zones was conducted as follows:

When the ratio of air void area to total area of the interval scanning surfaces of an element was greater than or equal to 50%, the element was assigned as an air-void element.

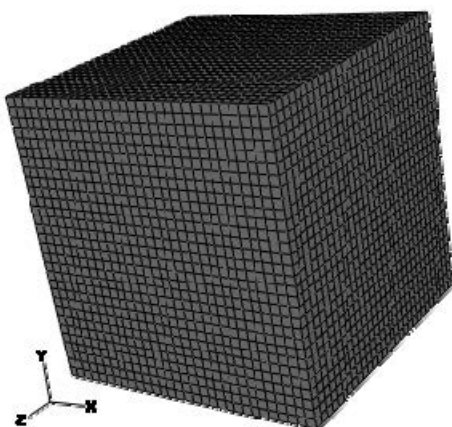


Figure 7: Element mesh for the heterogeneous part

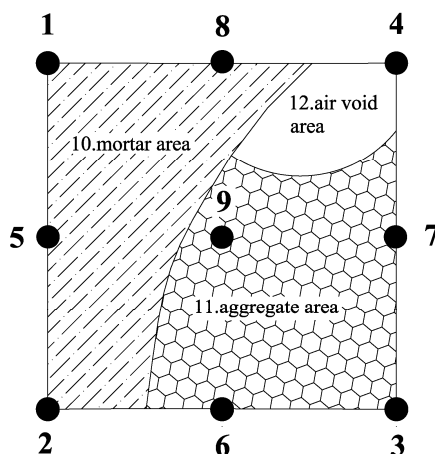


Figure 8: Twelve control factors for each scanning section in an element

If the eight nodes of an element were all in the area of aggregate, the element was assigned the material parameters of aggregate. If the eight nodes of the element were all in the area of mortar matrix, then the element was assigned the material parameters of mortar matrix.

If some of the eight nodes of the element were in the area of aggregate while other nodes were in the area of mortar matrix and the ratio of aggregate area to total area of the interval scanning surfaces of the element was greater than 55%, the element was assigned the material parameters of aggregate. Otherwise, the element was assigned the material parameters of mortar.

If the eight nodes were in the areas of different aggregates, the element was not an aggregate element but an interface element, and it was assigned the material parameters of the interface.

The heterogeneous composite part was divided into 27000 elements, including 9863 aggregate elements, 4514 mortar elements, 12530 interface elements and 93 air void elements. The aggregate volume fractions reached 36.5%, which was close to the real aggregate content (40%). Fig. 9 presents aggregate elements, interface elements, mortar elements and air void elements for the heterogeneous composite part.

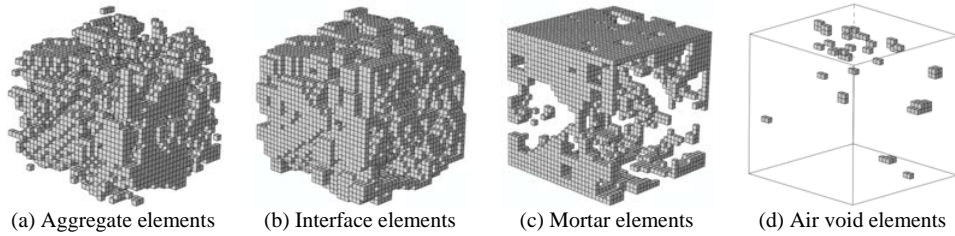


Figure 9: Aggregate elements, interface elements, mortar elements and air void elements for the heterogeneous composite part

## 4 Numerical simulation and discussion

### 4.1 Experiment processing of the concrete specimen

For comparison purposes, the four-point flexural-tensile experiment of the concrete specimen in Fig. 1(b) was conducted to investigate the mechanical behaviour of the concrete, including the crack initiation and propagation, the tensile strength of the concrete and the mid-span displacement. As shown in Fig. 10, a hydraulerservo-system machine was used to perform the four-point flexural-tensile experiment with a static loading speed of 0.05 mm/min.

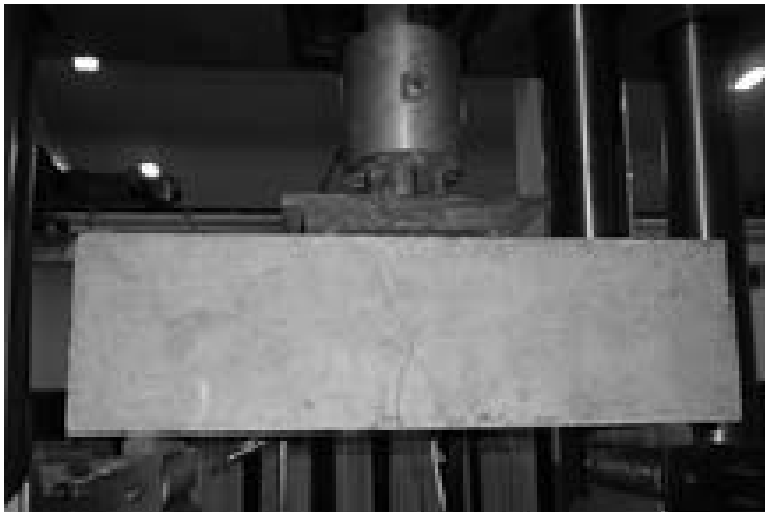


Figure 10: Experimental apparatus for the four-point flexural-tensile beam

### 4.2 Finite element numerical model of the concrete specimen

The specimen, shown in Fig. 1(b), is discretised into quadrilateral elements with 35541 nodes and 32800 elements. The  $xy$  and  $xz$  plane views of the FE mesh of the specimen are given in Fig. 11. The scanning zone was treated as a heterogeneous material, and each phase was identified by the method mentioned in section 3. The aggregate particles, mortar matrix, ITZ, and air voids are shown in Fig. 9. The remaining zones were treated as a homogeneous material, that is, isotropic concrete material. The boundary conditions and applied loads for the numerical model are identical with those for the experimental conditions.

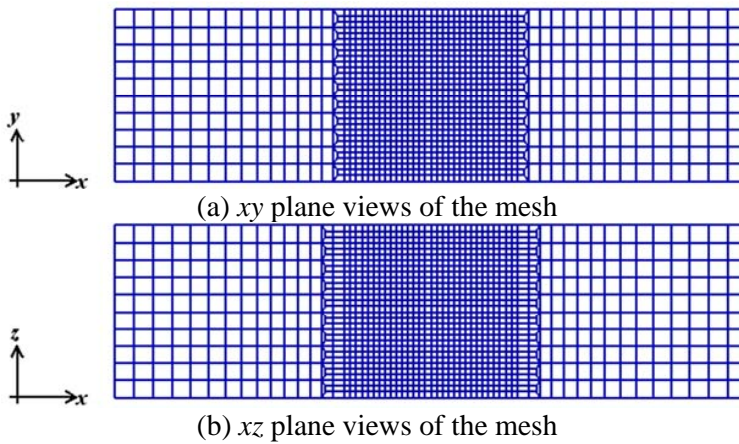


Figure 11: FE mesh of the specimen

### 4.3 Material constitutive model

The quasi-brittle-failure constitutive model (Stankowski, Runesson and Sture (1993)) for each material phase in the heterogeneous composite part was used to model the cracking failure of the aggregate particle, the mortar matrix and the ITZ. The cohesive forces can be expressed as:

$$\sigma(w) = f_t e^{-\alpha w}, \quad \alpha = \frac{f_t}{G_f}, \quad (1)$$

where  $f_t$  is the tensile strength of the material,  $w$  is the crack width, and  $G_f$  is the fracture energy. The nonlinear constitutive model for each phase of the composite used in the calculation is shown in Fig. 12; and the shaded zone is  $G_f$ .  $W_c$  denotes

the critical crack width. When the tensile strength of the material is reached, the damage begins to occur, but the crack width and the damage both are zero. If the crack width reaches to the critical crack width, the maximum damage occurs. The material parameters used in the analysis are given in Tab. 2. The parameters for both mortar matrix and aggregate particle phases are based on test results. However, it is quite difficult to determine the material properties of the ITZ. The only well-accepted idea is that the ITZ is the weakest link between the aggregate particle and the mortar matrix. It is normally weaker than the mortar matrix.

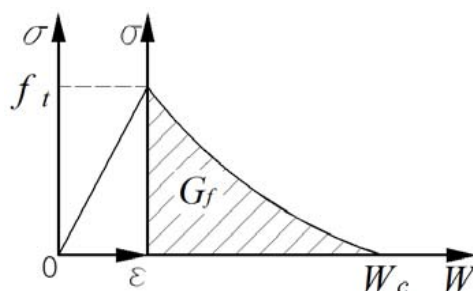


Figure 12: Stress-displacement curve

Table 2: Material properties used for numerical simulation

| Material zone | Elastic modulus (GPa) | Poisson's ratio | Tensile strength (MPa) | Critical crack width (mm) |
|---------------|-----------------------|-----------------|------------------------|---------------------------|
| Concrete      | 30                    | 0.17            | -                      | -                         |
| Mortar        | 26                    | 0.22            | 2.47                   | 0.096                     |
| Aggregate     | 55.5                  | 0.16            | 5.37                   | 0.096                     |
| ITZ           | 25                    | 0.16            | 1.16                   | 0.096                     |

#### 4.4 Comparisons of numerical and experimental results

Fig. 13 presents the two curves for the load and mid-span displacement: the line dotted with asterisks is the numerical simulation result from the reconstructed model, and the line dotted with solid circles is the experimental result. It can be observed that the two curves almost overlap in the elastic region. The failure load in the numerical simulation was 27.23 kN, which was very close to the 27.21 kN obtained in the experiment. It can also be observed that the two curves are very similar in the decreasing regions of the curves.

Fig. 14 shows the final crack shape and location at the front of the specimen. From the figure, we can see that the final crack shape and location obtained through the numerical and experimental methods are identical. In addition, Fig. 15 shows a large, penetrating crack at the bottom of the specimen. The crack location obtained in the numerical simulation is quite similar to that obtained by experiment method.

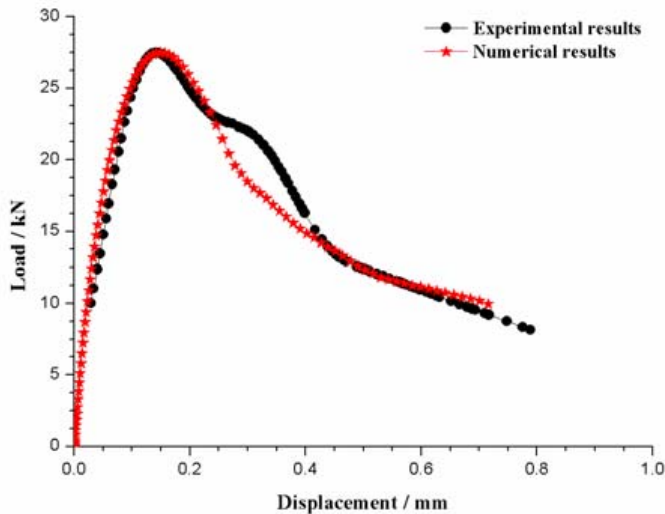
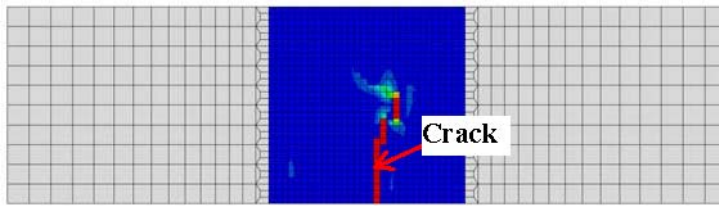
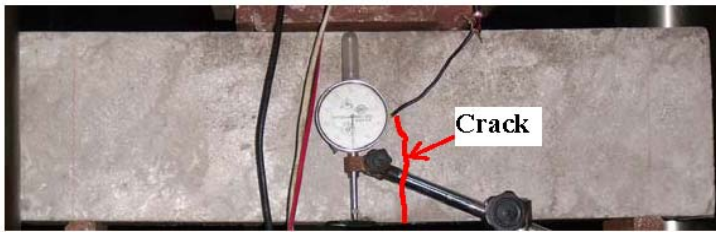


Figure 13: Curves of load and mid-span displacement

Fig. 16 shows a fracture surface of the specimen. From the figure, we can observe that the crack propagates not only through the mortar zones, but also through a few aggregate particles. As shown in Fig. 17, the damage development for each phase of material obtained from the numerical results is given. Red represents the most serious damage in Figure 17. The initial damage appears at the 25th loading step. At the period of initial damage, no damage can be observed in the aggregate particles and mortar matrix, but the minor damage, 5 failure elements, can be seen in the ITZ. When the applied load reached the critical load at the 53rd loading step, apart from the damage to the ITZ that can be seen, damage to aggregate particles and mortar matrix can also be observed. The obvious path of the macro crack in the mortar matrix and ITZ can be seen. At the phase of final failure, 234 failure elements for aggregate particles can be observed, 75 failure elements for mortar matrix, and 1012 failure elements for the ITZ. A main macro crack pattern can be found in this phase. Therefore, we can summarise that the crack initiation occurs in the ITZ; one macro crack is formed at final failure, and it is caused by the growth and propagation of the micro cracks.

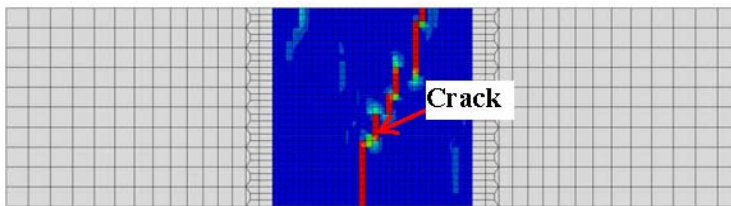


(a) Numerical result

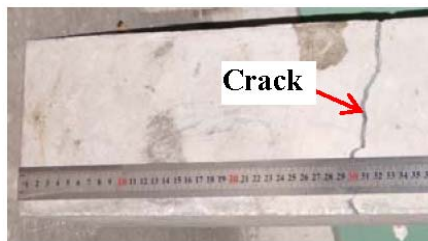


(b) Experimental result

Figure 14: Final crack shape and location at the front of the specimen



(a) Numerical result



(b) Experimental result

Figure 15: Eventual crack shape and location at the bottom of the specimen

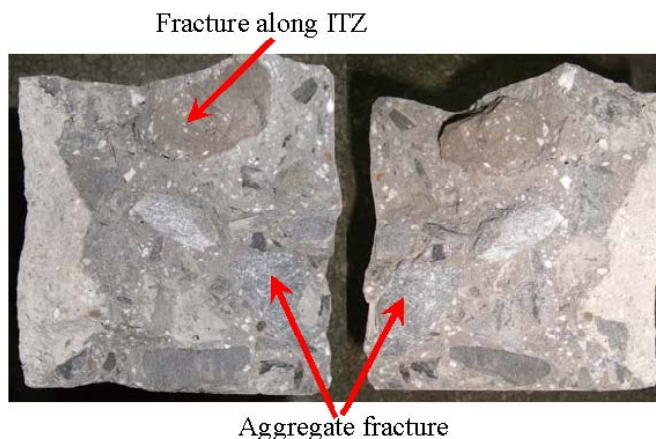


Figure 16: Fracture surface of the specimen

## 5 Conclusions

The main conclusions about the numerical analysis of concrete composites at the mesoscale based on 3D reconstruction technology using X-ray CT images are summarised here. X-ray CT is an effective technology for obtaining 2D slices of a concrete section. It is necessary to use morphology process technology to recover complete image information, including borders, and the median filtering method is an effective tool for eliminating potential impurities in the images. The volume data method is an effective method for reconstructing a 3D concrete model from X-ray CT images. The simple surface drawing method is a practical method for obtaining the interface between the aggregate phase and the mortar phase. The mapping mesh method has enough accuracy to generate a mesoscale finite element model reflecting the mesoscopic characteristics of aggregate, mortar, ITZ and air voids of concrete. Numerical simulations based on a reconstructed beam give a full load-displacement curve and a failure crack similar to those obtained from experiments. The damage development for each material phase obtained from the numerical results indicates that the crack initiation occurs in the ITZ; one macro crack is formed at final failure, and it is caused by the growth and propagation of the micro cracks.

**Acknowledgement:** The authors gratefully acknowledge support for this research from the National Natural Science Foundation of China (Grant No. 50779011, 11132003), the National Basic Research Program of China (973 Program, Grant No. 2007CB714104), and the Innovative Project for graduate students of Jiangsu Province (Grant No. CX10B\_202Z).

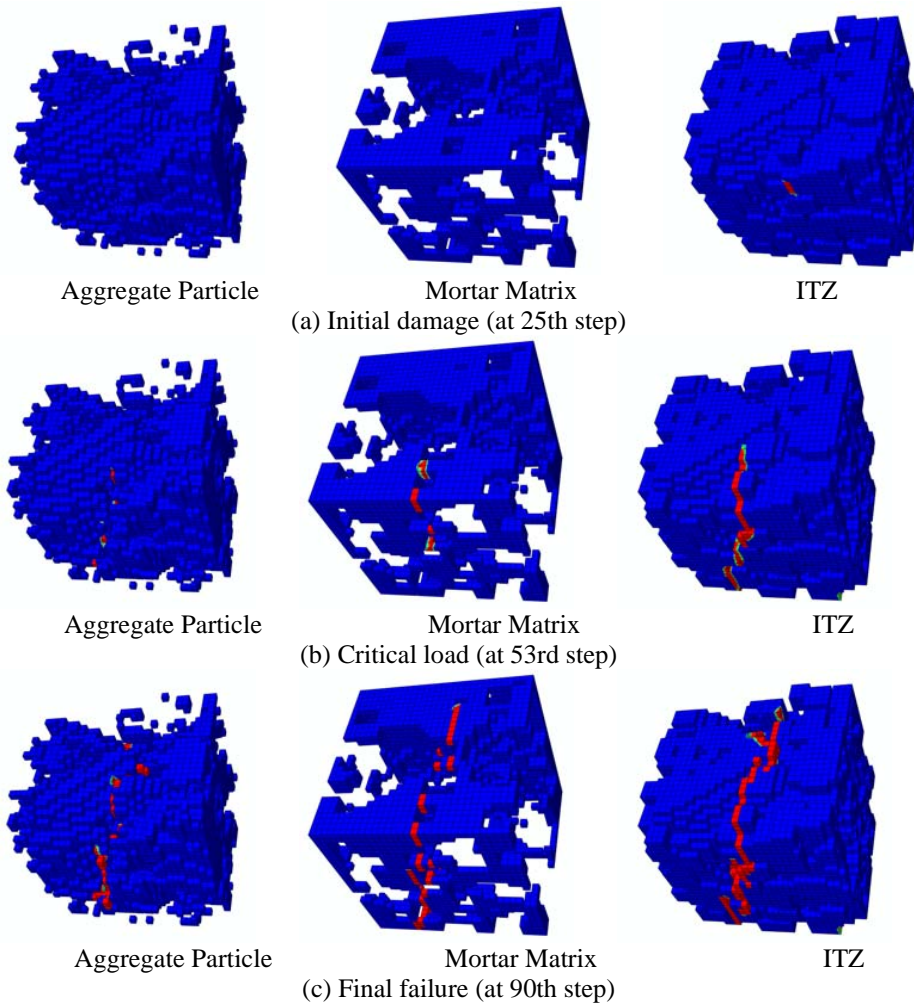


Figure 17: Damage development of each material phase

## References

- Andersson, L., Jones, A.C., Knackstedt, M.A., Bergström, L.** (2010): Three-dimensional structure analysis by X-ray micro-computed tomography of macroporous alumina templated with expandable microspheres. *J. Eur. Ceram. Soc.* Vol. 30, pp. 2547-2554.
- Buyukozturk, O.** (1998): Imaging of concrete structures. *NDT&E. Int.*, vol.31, pp.233-243.

**Cheok, G. S.; Stone, W. C.; Garboczi, E. J.**(2006): Using LADAR to characterize the 3-D shape of aggregates: preliminary results. *Cement. Concrete. Res.* Vol.36, pp.1072-1075.

**Du, C. B.; Sun, L. G.**(2007): Numerical simulation of aggregate shapes of two dimensional concrete and its application. *J. Aerospace. Eng.* Vol.20, pp.172-178.

**Evans, P. D., Morrison, O., Senden, T.J., Vollmer, S., Roberts, R.J., Limaye, A., Arns, C.H., Averdunk, H., Lowe, A. and Knackstedt, M.A. (2010):** Visualization and numerical analysis of adhesive distribution in particleboard using X-ray micro-computed tomography. *Int. J. Adhes. Adhes.* Vol. 30, pp. 754-762.

**Fu, G.; Dekelbab, W.**(2003): 3-D random packing of polydisperse particles and concrete aggregate grading. *Powder. Technol.* Vol.133, pp.147-155.

**Garboczi, E. J.; Bullard, J. W.**(2004): Shape analysis of reference cement. *Cement. Concrete. Res.* Vol.34, pp.1933-1937.

**Gonzalez, R.C.; Woods, R.E.; Eddins, S.L.**(2009): *Digital Image Processing Using MATLAB*. Gatesmark Publishing.

**Häfner, S.; Eckardt, S.; Luther, T.; Könke, C.**(2006): Mesoscale modeling of concrete: Geometry and numerics. *Comput. Struct.* Vol.84, pp.450-461.

**He, H.; Guo, Z.; Stroeven, P.; Stroeven, M.; Sluys, L.J.**(2009): Characterization of the packing of aggregate in concrete by a discrete element approach. *Mater. Charact.* Vol.60, pp. 1082-1087.

**John, S.L.; Denis, T.K.**(2001): Surendra P S. Measuring three-dimensional damage in concrete under compression. *ACI. Mater. J.* vol. 98, pp.465-475.

**Madadi, M., Jones, A.C., Arns, C.H., Knackstedt, M.A. (2009):** 3D imaging and simulation of elastic properties of porous materials. *Comput. Sci. Eng.* Vol. 11, pp. 65-73.

**Moar, C.E.; Kwan, A.K.H.; Chan, H.C.**(1998): Particle size distribution analysis of coarse aggregate using digital image processing. *Cement. Concrete. Res.* Vol. 28, pp. 921-930.

**Saaddeh, S.; Al-Rousan, T.; Garboczi, E.; Little, D.**(2005): Computations of particle surface characteristics using optical and X-ray CT images. *J. Comput. Mater. Sci.* Vol. 34, pp. 406-424.

**Shahidi, R., Tombropoulos, R., Grzeszczuk, R.P. (1998):** Clinical applications of three-dimensional rendering of medical data sets. *P. IEEE.* Vol. 86, pp. 555-568.

**Sobolev, K.; Amirjanov, A.**(2010): Application of genetic algorithm for modeling of dense packing of concrete aggregates. *Constr. Build. Mater.* Vol.24, pp.1449-1455.

**Stankowski, T.; Runesson, K.; Sture, S.**(1993): Fracture and slip of interfaces in cementitious composites. I: Characteristics. *J. Eng. Mech.* Vol. 119, pp.292-314.

**Tian, W.; Dang, F.N.; Liang, X.Y.; Chen, H.Q.**(2008): CT image analysis of meso fracture process of concrete. *Eng. J. Wuhan. Univ.* vol. 41,pp. 69-72. (in Chinese)

**Wang, Z.M.; Kwan, A.K.H.; Chan, H.C.**(1999): Mesoscopic study of concreteI: generation of random aggregate structure and finite element mesh. *Comput. Struct.* Vol. 70, pp. 533-544.

**Wittmann, F.H.; Roelfstra, P.E.; Sadouki, H.**(1985): Simulation and analysis of composite structures. *Mater. Sci. Engng.* Vol. 68, pp. 239-248.

**Wriggers, P.; Moftah, S. O.**(2006): Mesoscale models for concrete: Homogenisation and damage behaviour. *Finite. Elem. Anal. Des.* Vol. 42, pp. 623-636.

**Xu, N.W., Tang, C.A., Li, L.C., Zhou, Z., Sha, C., Liang, Z.Z., Yang, J.Y.**(2011): Microseismic monitoring and stability analysis of the left bank slope in Jinping first stage hydropower station in southwestern China. *Int. J. Rock. Mech. Min.* Vol. 48, pp. 950-963.

**Xu, R.; Yang, X. H.; Yin, A. Y.; Yang, S. F.; Ye, Y.**(2010): A three-dimensional aggregate generation and packing algorithm for modeling asphalt mixture with graded aggregates. *J. Mech.* vol. 26, pp. 165-171.

**Yang, R.; Buenfeld, N.R.**(2001): Binary segmentation of aggregate in SEM image analysis of concrete. *Cement. Concrete. Res.* Vol. 31, pp.437-441.

